Plasmon localization and field enhancement in flexible metasurfaces

Andrey Ivanov,[1,†] Igor Bykov,[1] Grégory Barbillon,[2,3] Konstantin Mochalov,[4,5] Denis Korzhov,[4,6] Alexander Kovalev,[4] Alexander Smyk,[7] Alexander Shurygin,[7] and Andrey K. Sarychev[1,*]

[1] *Institute for Theoretical and Applied Electrodynamics, Russian Academy of Sciences, Moscow 125412, Russia*
[2] *EPF-Ecole d'Ingénieurs, 55 Avenue du Président Wilson, Cachan 94230, France*
[3] *Sorbonne Université, CNRS, Laboratoire Interfaces et Systèmes Electrochimiques, LISE, UMR 8235, Paris 75005, France*
[4] *Shemyakin-Ovchinnikov Institute of Bioorganic Chemistry, Russian Academy of Sciences, Moscow 117997, Russia*
[5] *RUDN University, 6 Miklukho-Maklaya St, Moscow 117198, Russia*
[6] *National Research Nuclear University MEPhI Moscow 115409, Russia*
[7] *James River Branch llc, Tvardovsky st., 8, Moscow 123458, Russia*

(Received 5 August 2024; revised 2 November 2024; accepted 25 November 2024; published 17 December 2024)

We explore the optical properties of plasmon localization and local field enhancement in metal-plastic metasurface. The flexible metal-dielectric metasurfaces are made from modulated polycarbonate substrate coated by a thin silver film. Localization of an optical excitation is experimentally observed by near-field scanning optical microscopy within subwavelength areas in the regular open-resonator metasurface. The localized modes are seen as giant fluctuations of the local electric field spatially concentrated in hotspots, where the local field is much larger than the amplitude of the incident light. Local near-field spatial spectra consist of regularly distributed strong peaks. The maxima of the electric field are highly dependent on the sample structure. The form of the regularly distributed strong resonance peaks follows the topography obtained by atomic force microscopy. It is shown that strong electromagnetic field is concentrated in recesses where the silver film is typically thinner than on the bumps. This experimental observation is consistent with the results of computer simulations of a double-periodic metal-dielectric metasurface and the predictions of our analytical theory. It is found the silver nanofilm has strong adhesion to polycarbonate substrate.

DOI: 10.1103/PhysRevApplied.22.064064

I. INTRODUCTION

Optical resonators and metasurfaces assembled from them are relevant due to numerous applications in a variety of fields including photovoltaics and photodetectors [1,2], optical lenses and cloaks [3,4], near-field electromagnetic (EM) energy transfer [5], second- and third-harmonic generation [6,7], photocatalysis [8], refractive index sensing [9], plasmonic nanopainting [10,11], surface-enhanced Raman scattering (SERS) [12,13], and other applications, which are presented in detail in Refs. [14–16]. Metasurfaces typically consist of ordered or quasi(dis)ordered dielectric or plasmon nanoresonators whose size is smaller than the wavelength. Implementation of a powerful analytical tool, SERS spectroscopy, requires the creation of a resonant plasmonic metasurface that multiplies the incident EM field. Modern lithography technologies make it possible to obtain a variety of regular plasmonic surfaces with complex geometries. Such technologies include lithography using a focused ion beam [17] or an electron beam [18,19]. Low-cost technologies can be also employed as interference lithography (e.g., X-ray and UV [20–23]), nanoimprint, and nanosphere lithography [24,25]. It is noteworthy that multibeam interference lithography makes it possible to produce the large surface area filled with of the resonators at low cost [26]. The shape and geometry of the resonant metasurfaces determine the position of localized plasmon resonances and electromagnetic enhancement, which affects the sensitivity of SERS spectroscopy.

Metasurfaces for SERS have various unit cells. The simplest metasurface morphology is a one-dimensional (1D) periodic lattice with a sinusoidal profile or in the form of stripes or bars [26–39]. A 1D metasurface made of periodic Si(100) bars with a silver nanolayer was presented by Sarychev *et al.* [39]. The structure exhibits

*Contact author: sarychev_andrey@yahoo.com
†Contact author: av.ivanov@physics.msu.ru

unusual reflectivity behavior in the visible and near-IR spectral ranges due to excitation of dielectric resonances. Later, the work in [40] demonstrated that such a metasurface is effective for SERS applications by detecting 4-mercaptophenylboronic acid (MPBA) molecules immobilized on the surface due to its high Raman-to-luminescence (signal-to-noise) ratio. In addition, it was shown experimentally and theoretically that in such a structure, hybrid metal-dielectric resonances were realized, which manifested themselves in dips in the reflection. The possibility of realizing of a bound state in the continuum (BIC) in a hybrid plasmonic-photonic structure consisting of a plasmonic grating coupled to a dielectric optical waveguide with diverging radiation quality factor was explored in Ref. [41]. The authors theoretically demonstrated coupling of plasmonic and photonic resonances and increasing of quality factor in a silver relief grating coupled to a SiO_2 slab. SERS metasurfaces can be made of silicon-gold nanocones [42]. The metasurface, composed of the Si cones, show an enhancement of the local optical field and the SERS effect from 5.5-dithio-bis(2-nitrobenzoicacid) molecules, immobilized on silicon cones covered by gold nanoparticles. In this work, the authors developed the analytical theory of dielectric resonances excited in microcones, as well as computer modeling of the interaction of the dielectric microcone with gold nanoparticles. It was shown that the maximum SERS effect occurred when gold nanoparticles were not at the tip of the conical silicon resonator, but on the side wall, where dielectric resonances were excited. This effect is due to the hybridization of the dielectric and plasmon resonances predicted by computer simulations. The result corresponds to that obtained in the presented research.

A plasmon metasurface made of highly dense gold nanopolyhedrons (AuNPHs) was presented by Chen *et al.* [43]. The metasurface was obtained by self-assembly and it achieved SERS of about 1.7×10^6 for 4-aminothiophenol molecules. The Raman signals showed high homogeneity across the superlattice. The authors also demonstrated by both experiments and simulations that the surface-plasmon-induced hotspots are distributed uniformly across the surface, facilitating its application as flexible SERS sensors. Petty's group envisioned a metasurface in the form of periodic indentations in the form of inverted pyramids [44]. The gold metasurface was shown to be effective for SERS detection hepatitis A virus (HAV) and 4-mercaptobenzoic acid molecules. SERS reached 5×10^6 in this case at the wavelength 532 nm, which the metasurface is tuned for. The same authors report observation of the Shiga toxin via SERS. This toxin is often associated with dysentery.

A metasurface composed of gold octupolar nanostructures was proposed in Ref. [45]. SERS reached 9×10^7 due to the excitation of double plasmon resonance close to the laser wavelength of 785 nm. Caligiuri *et al.* proposed a metasurface made of a cellulose sheet covered by the silver nanolayer, where the arrays of holes were punched [46]. The authors demonstrated SERS from 1,4-benzenedithiol molecules. The Raman signal is six times larger in comparison with the silver-on-cellulose film. The sixfold enhancement is estimated for very few main Stokes lines while all other lines became detectable only when the holes are punched. Therefore, the array of holes allows the SERS signature of a benzenedithiol molecule to be obtained. Gabinet and Osuji presented a metasurface based on a vertical zinc oxide (ZnO) nanorod array covered by the gold surface layer. The 2×10^4 SERS was demonstrated from rhodamine 6G (R6G) molecules. The SERS was due to the tuning plasmonic nanorods to the excitation wavelength of 532 nm [47].

Yang *et al.* presented a metasurface made of the hexagonal array of gold nanoholes on the SiO_2 film with the mirror gold substrate. This metasurface was designed for SERS detection of benzenethiol molecules with SERS of about 10^6 [48]. Zhao *et al.* suggested a metal-dielectric metasurface consisting of layered particles, where gold layers are alternated with aluminum oxide layers. The absorption and scattering were demonstrated in the optical and IR range. SERS of 10^6 from 4-ATP molecules was reached by tuning nanorods to a wavelength of 785 nm [49]. Ma *et al.* fabricated the plasmonic metasurface whose optical properties can be changed by applying the constant voltage. Gold nanoparticles are deposited from an optical-electrochemical cell to the silver substrate covered by titanium nitride nanolayer that operates as the base electrode. The variation of electrode potential by less than 1 V led to increased density of deposited Au nanoparticles and decreased optical reflectivity from 93% to 1%. In this way, the base electrode gets blacker and blacker. SERS simultaneously increased by up to five orders of magnitude. SERS from 4-mercaptobenzoic acid molecules for the potential of 0.7 V was 10^5 times larger compared with SERS with the potential equal to zero charge (PZC) [50].

Kovalets *et al.* fabricated a metasurface by deposition of gold and silver on track membranes followed by its stretching. This approach allowed microcracks to be obtained in the metal layer, where the enhanced electric field was focused. The number of cracks increased with increasing the stretching. SERS from malachite green molecules was demonstrated [51]. Nguyen *et al.* presented a metasurface made of a silver mirror where polystyrene microspheres were deposited. The spheres are covered by the silver nanolayer. SERS of 10^8 was obtained from R6G molecules deposited on the metasurface [52]. Zhang's group realized a broadband SERS substrate for the detection of R6G molecules consisting of a plasmonic metasurface composed of large silver nanoparticles on which small aggregates of silver were obliquely deposited. SERS of 10^7 was achieved due to the matching of the broadband plasmonic resonance in the metasurface with resonance in the silver aggregates [53]. Wang *et al.* presented a plasmonic metasurface fabricated as silver nanocube arrays with an average intercube gap of about 1 nm. The giant fields, generated in the gaps, result in SERS of 10^7. Crystal violet molecules, the drug lidocaine, and methotrexate were detected using the cubic metasurface [54]. Luo *et al.* presented a plasmonic metasurface made by size-tunable adhesion lithography from parallel nanogap arrays containing 100 million ring-shaped nanogaps of controllable diameter, width, and pitching. SERS for R6G molecules is reported to reach 10^8 due to collective plasmon resonance [55]. Bauman *et al.* presented a plasmonic metasurface based on gold nanospheres with a tunable nanogap between them [56]. They declared that tunable gap plasmonic metasurfaces generate a field enhancement of the order of 10^4 over measurements on bare silicon substrate.

Zhang *et al.* presented a plasmonic metasurface consisting of the array of sub-10-nm chiral nanogaps between nanocrescents [57]. There is a strong plasmonic coupling between gaps and tips, which results in circular dichroism (CD) activity. Such a metasurface is used to detect L-cysteine and D-cysteine molecules absorbed on the chiral nanogaps. It was shown that chiral nanogaps with a gap size of 5 nm were optimal for the SERS detection due to their CD activity and *g*-factor. These L-chiral nanoslits allowed the SERS spectrum of L-cysteine to be obtained with more-intense peaks than that of D-cysteine, and R-chiral nanoslits allowed the SERS spectrum of D-cysteine to be obtained with more intense peaks than that of L-cysteine. Thareja *et al.* presented an anisotropic plasmonic metasurface consisting of an array of parallel nanogrooves in the gold film [58]. It was proposed that gap plasmons, excited in the metasurface, generate enhanced electric fields in controlled directions. Using such a metasurface, Raman peaks (G and 2D) of graphene were studied, which were found to be enhanced by a factor of 25–50. Jiang *et al.* fabricated a plasmonic metasurface made of gold-coated silicon nanoflowers for SERS detection of benzoic acid molecules. SERS of 10^6 was achieved by the exciting enhanced electric fields between the petals of the nanoflowers [59]. Flexible metasurfaces are of particular interest [29,60–63] due to their benefits compared with rigid substrates [64,65].

Indeed, flexible metasurfaces can be employed on irregular surfaces for *in situ* biodetection, thus surmounting the issues associated with complex analyte extraction. Furthermore, this flexibility of the substrates can enable the realization of sensors in the form of patches, which can be deposited on skin and on facial masks for continuous tracking [60]. Choo's group has created a flexible metasurface of quasi(dis)ordered metal-insulator-metal (MIM) disk-shaped nanostructures whose electromagnetic hotspots are spatially controlled, and also allow the Raman background signals coming from the polymeric substrate to be blocked [62]. This flexible metasurface enabled the detection of uric acid in human tears in its physiological concentration range (25–150 μM) at a level comparable to a commercial enzyme-based assay. Barman's group presented plasmonic nanostructures composed of multiple alternate stacks of silver and silica [60]. This plasmonic nanostructure enabled a first resonance to be obtained close to the excitation laser beam allowing a large Raman enhancement, and thus a SERS detection of the fusion protein of SARS-CoV-2 and H1N1 at a concentration of 500 nM. We developed the analytical theory as well as experimental observation of the plasmons excited in open resonators formed by a metal-dielectric metasurface [26]. In the theory, the conformal mapping is used, which is similar to the mapping used by Pendry's group to transform one side metal grating into a rectangular metal slab [27,66–68]. The metal-dielectric metasurface, investigated in Ref. [26] is composed of a modulated dielectric coated by a thin silver layer, permitting the matching of plasmonic resonances to the excitation wavelength of 785 nm.

To summarize the above brief review, SERS metasurfaces can operate either as a system of nanogaps between metal particles of different sizes and shapes or as modulated metal surfaces. In the latter case, the metasurface operates as a system of open plasmon resonators. Hybrids are also considered. For example, silver-on-cellulose film where microholes are punched is suggested to detect benzenedithiol molecules [46]. The highest SERS is achieved when the nanogaps are filled with the molecules under study. Yet, the highly concentrated gap field could easily damage large organic molecules. On the other hand, regular metasurfaces seem more suitable for detecting viruses and other biological micro-objects or, say, microplastic contaminants.

In this work, we investigate the optical properties of the flexible metal-dielectric metasurfaces fabricated from modulated polycarbonate substrate coated by a thin silver film. First, we explore the optical properties by using computer simulations and our analytical theory. Then, we explore them experimentally by employing the measurement of the absolute reflection and ellipsometry as well as those of scanning near-field optical microscopy (SNOM). The developed flexible metasurface concentrates the incident light into subwavelength hotspots. The effective size of a hotspot could be 10 times less than the wavelength. The manufacturing process is based on usual photolithography and, therefore, it is suitable for the mass production. The proposed plasmonic metasurface is 2D, unlike the widely represented metasurfaces with 1D periodic lattice. It is periodic in two directions, i.e., has square symmetry and its optical properties do not depend on the light polarization when the light is incident normal to the metasurface. The proposed metasurface is flexible, which provides additional possibilities for use on uneven surfaces. Moreover, such regular metasurfaces are easily optimized for tuning to the required wavelength, which opens up the prospect of creating highly selective SERS sensors.

II. COMPUTER SIMULATIONS OF FLEXIBLE METASURFACES

Here, we examine 1D periodic metal gratings supporting localized plasmons. The metal grating with two-side modulation efficiently concentrates and stores electromagnetic energy [see Fig. 1(a)]. The local electric field is enhanced resonantly, and the localized plasmons are calculated analytically in our work [26] using the quasistatic approximation for the nanogratings whose dimensions (thickness and modulation) are much smaller than the wavelength λ. Full-scale computer simulations are performed of 1D and 2D metal gratings. The resonance condition for resonance thickness $d_r^{(n)}$ at the film bumps is determined by the following equation coming from Ref. [26]:

$$d_{r,\max}^{(q)} = \frac{L}{2\pi} \ln \left[\frac{\left(\frac{(\varepsilon_1-\varepsilon_{m1})(\varepsilon_d-\varepsilon_{m1})}{(\varepsilon_1+\varepsilon_{m1})(\varepsilon_d+\varepsilon_{m1})} \right)^{\frac{1}{2q}} - \tanh \frac{h_1}{2}}{1 - \tanh \frac{h_1}{2}} \right], \quad (1)$$

where L is the period, $h_1 = h(2\pi/L)$ is the dimensionless film modulation, $h = x_{\max}^{(f)} - x_{\min}^{(f)}$ is shown in Fig. 1, and ε_m, ε_d, and ε_1 are the permittivity of the metal, dielectric, and the front medium, respectively. Here $q = 1, 2, 3, \ldots$ is the order of the resonance (see Fig. 2). In our previous investigation [26], we considered modulated film, the thickness of which is highest at the top (bumps) but lowest in the depressions (dents) denoted by a star in Fig. 1(a). The minimal thickness of the modulated resonance film is equal to

$$d_{r,\min}^{(q)} = \frac{L}{2\pi} \ln \left[\frac{\left(\frac{(\varepsilon_1-\varepsilon_{m1})(\varepsilon_d-\varepsilon_{m1})}{(\varepsilon_1+\varepsilon_{m1})(\varepsilon_d+\varepsilon_{m1})} \right)^{\frac{1}{2q}} + \tanh \frac{h_1}{2}}{1 + \tanh \frac{h_1}{2}} \right]. \quad (2)$$

Equations (1) and (2) determine the range of the film thickness that gives the plasmon resonances. The resonance conditions give the relation between resonance thickness $d_{r,\max}^{(n)}$, and $d_{r,\min}^{(n)}$, period L, modulation depth h, and permittivities ε_d, ε_1, and ε_m for a such periodic grating [Fig. 1(a)]. The resonance thicknesses $d_{r,\max}^{(1)}$ and $d_{r,\min}^{(1)}$ for realistic parameters of the silver grating on glass substrate ($\varepsilon_d = 2$, $\varepsilon_m = \varepsilon_{\mathrm{Ag}}(\lambda = 785\ \mathrm{nm}) = -30 + 0.4\,i$; [69]) for a fixed wavelength of $\lambda = 785$ nm are shown in Fig. 1(b).

The theory that we developed in Ref. [26] predicts that the local electric field concentrates in a dent of the modulated metal film. Our theory is based on the conformal mapping from the $z = x + iy$ frame to $w = \exp z + x_0$, where $x_0 = \tanh(h_1/2)$, h_1 is the dimensionless modulation. In the w frame, the modulated metal film transforms into a cylinder which can be solved exactly using the quasistatic approximation. Then, we apply the inverse transformation $w \to z$. The plasmon resonances in the metal cylinder correspond to the resonances in the modulated film. The field maxima, distributed over the metal cylinder, map to the field maxima in the film. The field amplitude $|E(x,y)|^2$ in $\{x,y\}$ frame includes the square of the Jacobian of the conformal mapping $|dw/dz|^2 = |dz/dw|^{-2} = |w - x_0|^2$. The coordinate w is equal to $w = \exp i\varphi$ at the front interface of the film. The coordinate $x_{\max}$, where the

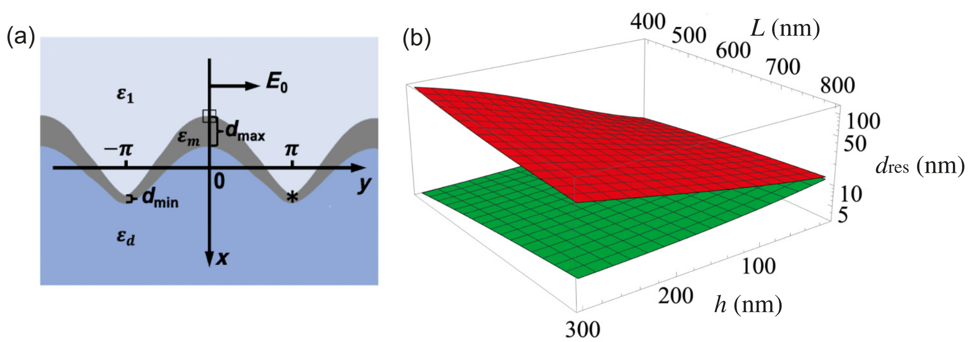

FIG. 1. (a) The design of a plasmonic grating based on a metal film with permittivity ε_m and thickness d deposited on the modulated dielectric substrate (shown in dark blue) with permittivity ε_d, where "y"-polarized light is incident from top; the star "$*$" denotes the point with dimensionless x, y coordinates $x = x_{\max}^{(f)}/(2\pi/L)$ and $y = \pi$, where the film thickness is minimal $d = d_{\min}$ (dent) and surface electric field is at a maximum; the small open square "□" denotes the point with coordinates $x = x_{\min}^{(f)}/(2\pi/L)$ and $y = 0$, where the film thickness is maximal $d = d_{\max}$ (bump) and surface electric field is at a minimum, the film modulation $h = x_{\max}^{(f)} - x_{\min}^{(f)}$. (b) Resonance thickness $d_{r,\max}^{(1)}$ (red curve) and $d_{r,\min}$ (green curve) of modulated silver film as a function of period L and modulation depth h for dipole resonance ($q = 1$) at wavelength $\lambda = 785$ nm; $\varepsilon_d = 2$, silver $\varepsilon_m \simeq -30 + 0.4\,i$ (at $\lambda = 785$ nm).

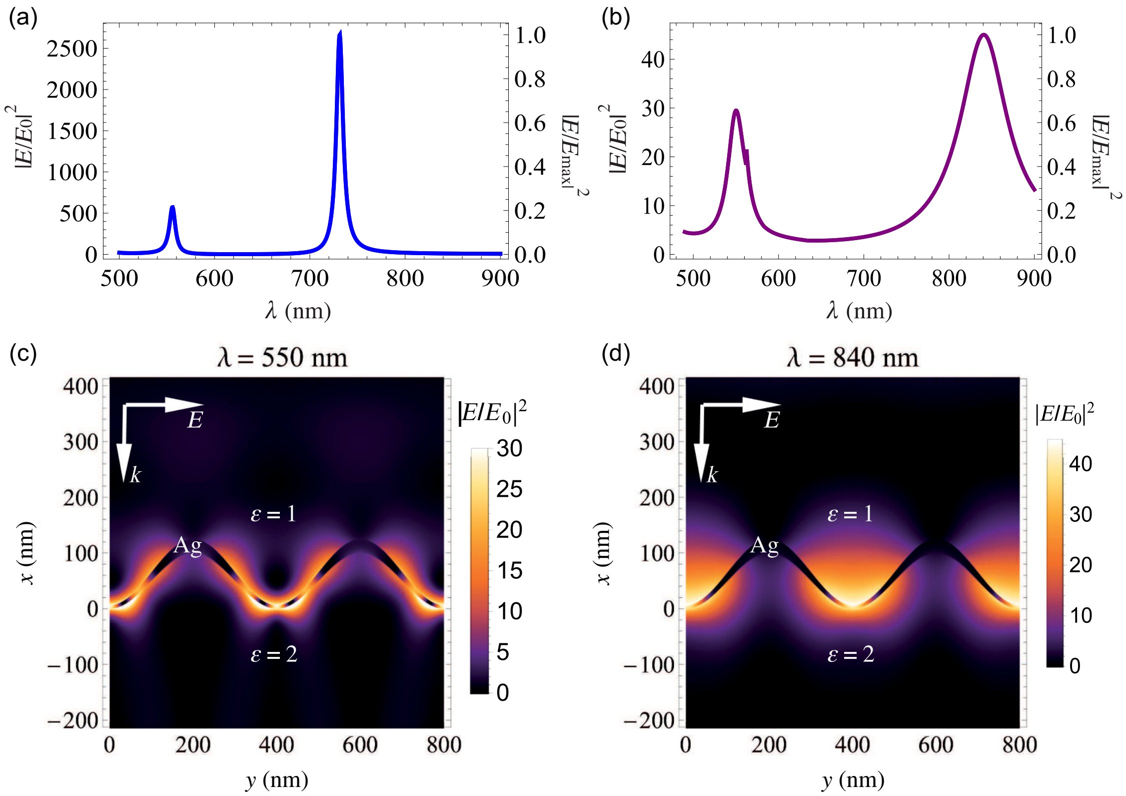

FIG. 2. Theoretical electric field intensity in 1D modulated metal film (see Fig. 1) (illumination under normal incidence): (a) analytical results and (b) computer simulations. Distributions of the electric field intensity corresponding to two resonances displayed in Fig. 2(b): (c) $\lambda = 550$ nm and (d) $\lambda = 840$ nm, where the silver film parameters are $L = 400$ nm, $h = 100$ nm; $d_{max} = 25$ nm, and $d_{max}/d_{min} = 4$. Analytical left (a) and numerical left (b) axes of electric field intensities correspond to absolute values of electric field intensities. Analytical right (a) and numerical right (b) axes of electric field intensities are normalized by their respective maximum values at the wavelengths of 730 and 840 nm.

field is maximal, corresponds to $\varphi = (2p+1)\pi$; the coordinate x_{min}, where the field is minimal, corresponds to $\varphi = 2p\pi$ $(p = \pm 1, 2, 3, \dots)$. Therefore, the ratio of the field in the dents and on the bump is proportional to

$$\frac{|E_{max}|^2}{|E_{min}|^2} \propto \frac{1+x_0}{1-x_0} = \exp\left(\frac{2\pi h}{L}\right). \tag{3}$$

We obtain that the dent field is five times larger than the bump field when the modulation $h = L/4$ as shown in Fig. 2. The field intensity in the maximum estimates for the film where thickness h is much smaller than the period L of the modulation is as follows:

$$|E_{max}^{(q)}|^2 \sim Q_m^2 \left(\frac{\pi h}{L}\right)^{2q}, \tag{4}$$

where $Q_m = |\varepsilon_m|/\Im\varepsilon_m$ is the metal quality; it is also assumed that $|\varepsilon_m| \gg 1$. For example, the silver quality $Q_m \sim 10$–10^2 in almost all optical and near-infrared spectral ranges. The above esteem gives a significant enhancement of the local electric field even for a modest film modulation. Therefore, a thin modulated metal film can be considered as a simple but effective open plasmon resonator for light energy concentration in hotspots. Here, we examine plasmonic properties of the real, flexible metal films well suitable for mass production. First, we investigate how the uneven thickness of the metal coating affects the resonant frequencies. The amplitude of the local field $|E/E_0|^2$ is found from the direct numerical solution of the Maxwell equations in the COMSOL environment (E_0 is the electric field of the incident light). The model was set up for one unit cell of the grating, flanked by Floquet boundary conditions describing the periodicity. We simulate the electric field enhancement in the modulated thin metal film with period $L = 400$ nm and amplitude of the modulation $h = 100$, 150, and 200 nm, for different ratios $d_{max}/d_{min} = 3.8$ and 2, and $d_{max} = d_{min}$, which means that the metal film is uniform in length (here d_{max} is the metal thickness at the grating bumps, d_{min} is the metal thickness at the grating dents). Let us assume that a transversely polarized wave is incident normally on a silver grating from a medium with a dielectric permittivity of 1, and the grating itself is located on a substrate with a dielectric permittivity of 2. The typical electric field distribution in dipolar and multipolar plasmons for this configuration is shown in

Fig. 2, for $L = 400$ nm, $h = 100$ nm, and $d_{\max} = 25$ nm ($d_{\max}/d_{\min} = 4$).

The result of the computer simulation is in agreement with the analytical results shown in Fig. 2(a). The analytical, quasistatic theory was developed in our previous investigation [26]. When the grating is excited by the incident light, the surface electric field is much enhanced. The quasistatic theory qualitatively describes the field enhancement even in the nonquasistatic case $kL \simeq 5$, where $k = 2\pi/\lambda$ is the wavevector, estimated for $\lambda = 600$ nm. We believe the theory can be used for the estimations, since the field is concentrated in the nanograting whose thickness and modulation are smaller than wavelength. The lateral size of a plasmon maxima is of the order of the film period L. The radiation loss, which is proportional to $Ld_{\min}k^2$ remains less than one. For example, for silver film with parameters $L = 400$ nm, $h = 100$ nm, $d_{\max} = 25$ nm, $d_{\min} = 6$ nm, and $\lambda = 600$ nm (see Fig. 2), the radiation loss $Ld_{\min}k^2 \simeq 0.3$. Yet, the radiation loss decreases the absolute value of the local field enhancement, as shown in Figs. 2(a) and 2(b) (left axis). Figures 2(a) (right axis) and 2(b) (right axis) show relative values of the local field enhancement with respect to their maximum values. It can be seen from Figures 2(a) and 2(b) that there is an agreement between the analytical and numerical calculations at the wavelength of 550 nm, while at the wavelength of ~840 nm, there is more significant difference. We speculate that the radiation loss is less for the quadruple resonance at 550 nm [Fig. 2(c)] than for the dipole resonance at 840 nm [Fig. 2(d)]. Indeed, electric currents are directed in opposite directions in the quadruple plasmon and, therefore, they partially cancel their radiation. We further show in Sec. IV that the theoretical results are in agreement with our SNOM experiment.

Figure 3 shows a computer simulation of the absorption and electric field intensity as a function of the wavelength and different ratios of silver thickness. It can be seen that the maximum electric field is concentrated in dents, where the silver thickness is smallest. The position of the resonances strongly depends not only on the film thickness, but also on the ratio $d_{\max}/d_{\min}$ along the entire length of the film. For instance, for $\lambda = 785$ nm, $L = 400$ nm, and $h = 100$ nm, the resonant maximum film thickness is around 35–40 nm if the film thickness at the bump is four times greater than the film thickness at dents [Figs. 3(a)–3(c)]. This case corresponds to the results of the quasistatic theory. The resonant maximum film thickness is approximately 20–25 nm for the same film parameters, if the film thickness at the top is twice that in the cavities [Figs. 3(d)–3(f)]. If we assume that the metal film is evenly distributed along its entire length, then the resonant thickness becomes even smaller [Figs. 3(g)–3(i)]. The maximum absorption corresponds to the maximum of electric field and reaches 40–60% [Figs. 3(j)–3(o)]. In Figs. 2(b) and 3 a narrow band in the intensity of the electric field can be seen at a wavelength of 563 nm, which is close to $\approx L/\sqrt{\epsilon_d}$. We speculate that the anomaly is associated with the Wood anomaly due to the diffraction in dielectric with permittivity $\epsilon_d = 2$ from the structure with period $L = 400$ nm. The enhancement of the electric field intensity in the described simple metal film can be improved significantly by increasing the ratio $d_{\max}/d_{\min}$, as well as by including an additional metal sublayer, as was proposed in Ref. [70]. The results obtained are important from a technological point of view, since by choosing the method and mode of metal deposition on the modulated surface, one can control the resonant characteristics of the plasmonic grating.

III. EXPERIMENTAL DETAILS OF FLEXIBLE METASURFACES

Industrial polycarbonate can be an excellent basis for the production of resonator metasurfaces. Polycarbonate is a thermoplastic polymer that contains carbonate groups in its chemical structures. It is a crystal clear, colorless, amorphous engineering thermoplastic notable for its high impact resistance. The advantages of using polycarbonate are its flexibility and ability to create special shapes over a wide temperature range. Ultimate tensile strength is 55–75 MPa, Young's modulus of elasticity is 2.2–2.4 GPa, and flexural strength is 90–120 MPa. In practice, this means that polycarbonate-based metasurfaces bend well and can be mounted on any surface or used as wearable devices. Another feature is limited chemical resistance to numerous aromatic solvents, including benzene, toluene, and xylene. Melting point of polycarbonate is around 300 °C, but it already begins to change its properties at a temperature of 125 °C. This property can be used to additional enhancement of SERS signal by changing the shape of the metal-polycarbonate composition when heated by laser radiation of the required power.

A. Fabrication of flexible metasurfaces

Flexible metasurfaces were fabricated from modulated flexible polymer substrate coated by a thin silver film [see Fig. 4(a)]. Metasurfaces is produced by holographic lithography technique in accordance with the technology described in one of our previous works [26], where a periodic structure was formed directly on a photopolymer film. The recording setup used a spatial light modulator HED-6001 (monochrome LCoS reflective display), and an ultraviolet laser ($\lambda = 405$ nm). Then, the (Shipley S-1813) positive photoresist was sputtered on a 4-in. (10.16-cm) silicon wafer. The exposure dose in the lithographic device was varied from 4.1 to 8.5 $\mu J/cm^2$. Next, the wafer was developed in a solution of Microposit 303A developer and 15%*DI* water and dried by centrifuge at 4000 rpm.

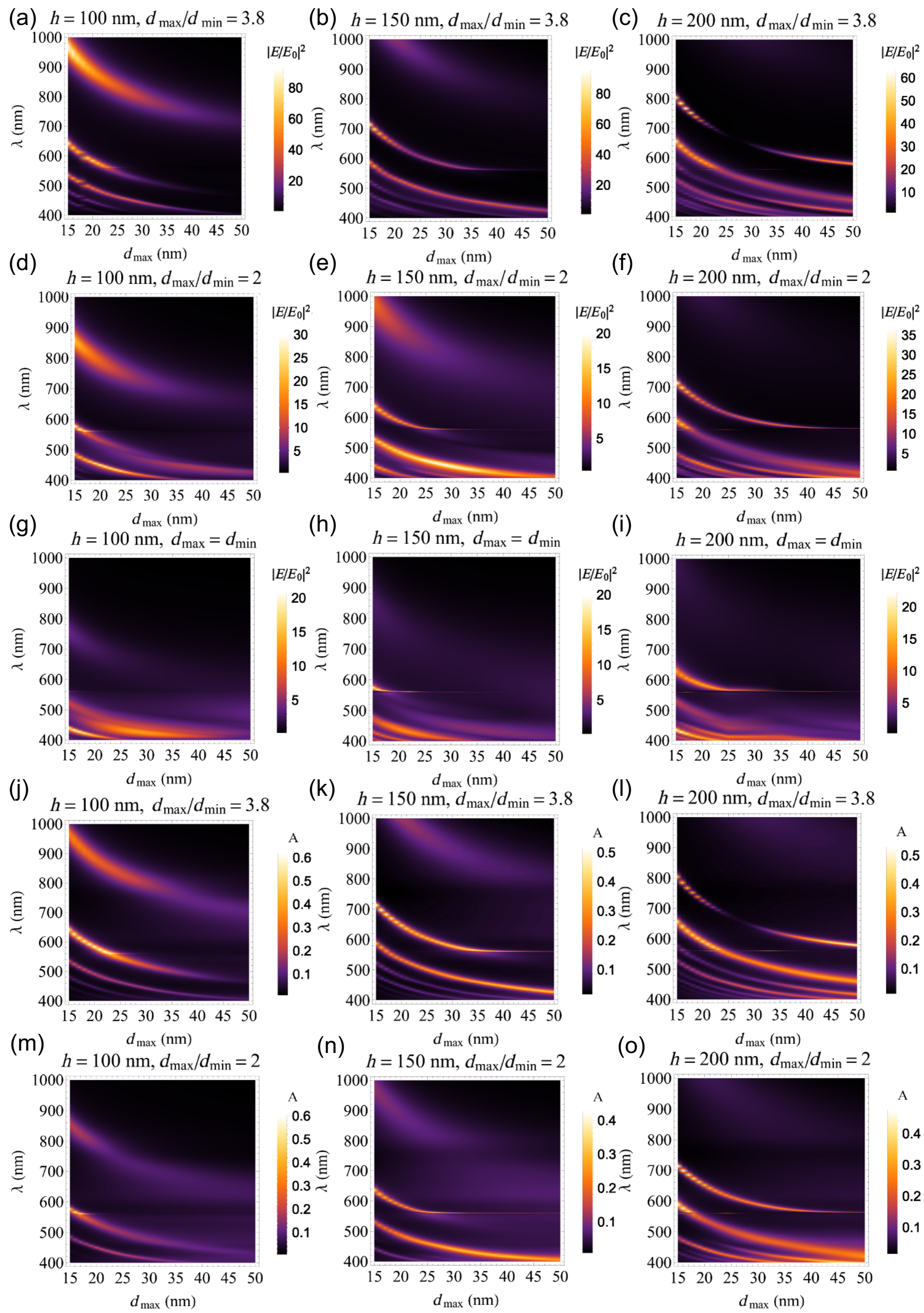

FIG. 3. The enhancement of the electric field in 1D modulated thin silver film (Fig. 1) with period $L = 400$ nm, and varying ratio d_{max}/d_{min} and modulation amplitude h. Ratio $d_{max}/d_{min} = 3.8$: (a) $h = 100$ nm, (b) $h = 150$ nm, and (c) $h = 200$ nm. Ratio $d_{max}/d_{min} = 2$: (d) $h = 100$ nm, (e) $h = 150$ nm, and (f) $h = 200$ nm. Ratio $d_{max}/d_{min} = 1$: (g) $h = 100$ nm, (h) $h = 150$ nm, and (i) $h = 200$ nm. Absorption in the modulated thin metal film with period $L = 400$ nm, and varying ratio d_{max}/d_{min} and modulation amplitude h. Ratio $d_{max}/d_{min} = 3.8$: (j) $h = 100$ nm, (k) $h = 150$ nm, and (l) $h = 200$ nm. Ratio $d_{max}/d_{min} = 2$: (m) $h = 100$ nm, (n) $h = 150$ nm, and (o) $h = 200$ nm.

The experimental thickness of the silver coating was determined as follows: silver was sputtered from a molybdenum crucible for 1.5 min using electron-beam heating at a current of 40 mA and a voltage of 8 kV. The silver was deposited on the transparent plate as well on the modulated polycarbonate surface. The thickness of the silver layer sputtered on the transparent plate was estimated by the transmission in the optical channel of the test sample at a wavelength of 600 nm. In the process of the deposition, the transmittance decreased to almost

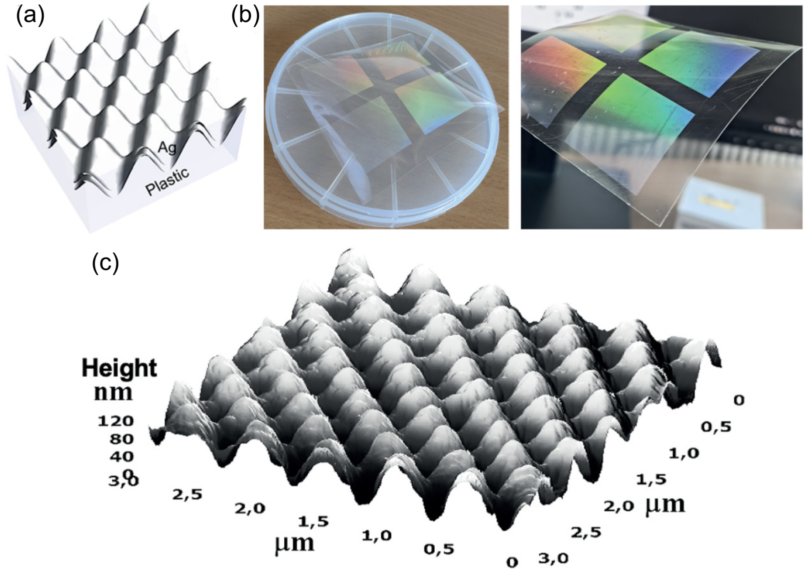

FIG. 4. (a) Sketch of the 2D metal-dielectric metasurface fabricated from modulated flexible polymer substrate covered by a thin silver film; this structure is used in our computer simulations. (b) Pictures of flexible metasurfaces before the silver deposition. Colored areas demonstrate diffraction of reflected natural light as it passes through the metasurface. (c) AFM image of the 3D topography of the metasurface with a period $L = 400$ nm, and a maximum metal top thickness of $\sim$65 nm.

zero, which corresponded to a silver thickness of 110 nm. It was worth noting that the silver thickness of 110 nm corresponded to the thickness of the plane silver layer. The thickness of the witness silver film, deposited on the plane glass plate, gave an important indicator to control the deposition process. The silver was distributed unevenly on the structured polycarbonate surface. For the maximum thickness $d_{\max} = 65$ nm and the ratio $d_{\max}/d_{\min} = 5$, we observed a good agreement between the experimental and theoretical reflectances, as shown in Fig. 5.

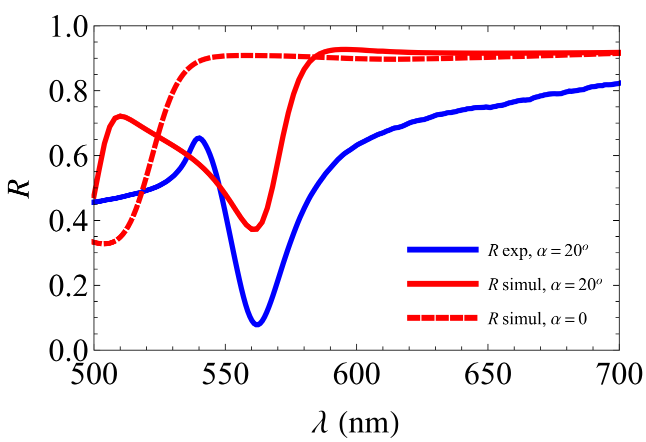

FIG. 5. Reflectance from metasurface with structure shown in Fig. 4. Comparison between experiments (blue line) and computer simulation (red lines) of 2D metasurface for the silver thickness of $d_{\max} = 65$ nm. Here α is the angle of incidence relative to the normal.

The metasurfaces with a period L of 400 nm and modulation amplitude from 100 to 200 nm were fabricated. Pictures of fabricated flexible metasurfaces are shown in Fig. 4(b). Limited space structure forming was applied to minimize volume shrinkage of the plastic material which is of high importance for dimensional stability and local field properties. The surface profile is also important and the technology has been designed to get it closer to that obtained theoretically. The morphology of the fabricated metasurfaces was measured by atomic force microscopy [AFM; see Fig. 4(c)].

B. Optical characterizations: scanning near-field optical microscopy, ellipsometry, and reflectance

For the electric field distribution, an aperture near-field optical microscopy was employed using an original setup named “System for probe-optical 3D correlative microscopy” of the IBCh RAS (see http://ckp-rf.ru/usu/486825/). Illumination was carried out by the far-field, and detection was carried out by the near-field, as can be seen from Fig. 6. The measurements are carried out using the shear-force method. The resonant frequency is 32 kHz. The tip oscillates in the x–y plane. Due to feedback, the distance between the probe and the sample surface was maintained constant. Scanning was performed with a platform for x–y micropositioning. An argon laser with the wavelength of 514.5 nm was used for excitation, and the incident power on the sample was 10 μW. The beam diameter was approximately 1 mm. The incidence angle was approximately 60° to the normal. This

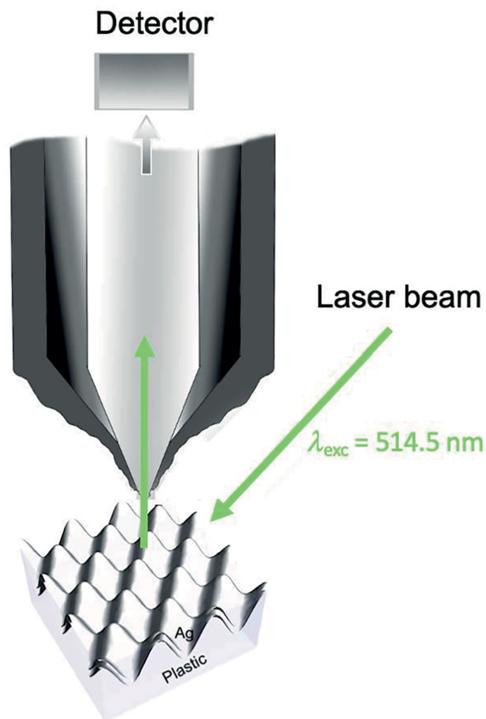

FIG. 6. Principle scheme of SNOM measurements.

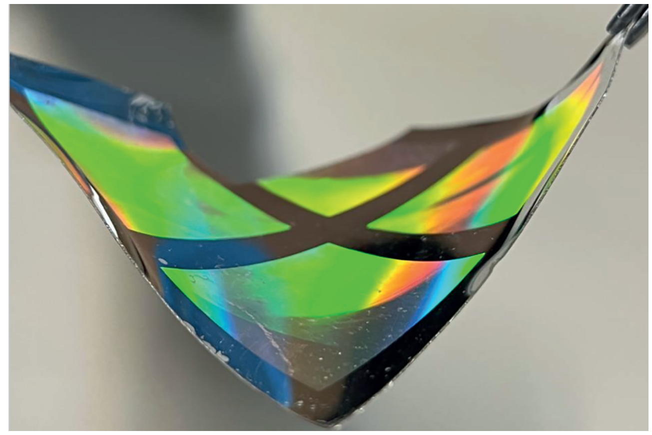

FIG. 7. Silver-coated flexible metasurface with the structure displayed in Fig. 4.

angle was determined by the design features of the installation. Nufern 460-HP single-mode fiber with an aperture of less than 100 nm was used as a radiation receiver. Detection was carried out using an Andor Shamrock 750 monochromator and an Andor DU971P-BV CCD camera. Topography scans using the shear-force and SNOM methods were performed sequentially one after another. Topography scanning parameters were 512×512 pixels and scanning frequency of 0.5 Hz (pass time for one line of 2 s). SNOM image parameters were 60×60 pixels and an exposure time at each point of 0.5 s. To determine the macroscopic optical properties of flexible metasurfaces, a spectroscopic ellipsometer SE 850 DUV (Sentech, Germany) is used. First, the absolute value of the reflectance is measured for the incidence angle $\alpha = 20^\circ$, close to the normal. The measured reflectance from metasurface and its comparison with the computer modeling are presented in Fig. 5. The angular ellipsometric parameters $\Psi(\lambda, \alpha)$ and $\Delta(\lambda, \alpha)$ are measured by the same ellipsometer in the range of the angle of incidence α from 20° to 70°. The "anomalous" behavior of Ψ and Δ give the position of the polarization anomaly in $\{\lambda, \alpha\}$ plane.

C. Metasurface flexibility

The flexibility of silver-coated metasurface is displayed in Fig. 7. To check the degree of flexibility, the following experiment was performed. A 34×34 mm^2 square section containing a periodic metasurface was cut out. First, the reflectivity of the sample before bending was measured. The sample was fixed in a holder to straighten it. The holder was fixed on an optical table and illuminated by a laser beam coming from a helium-neon laser. The parameters were laser wavelength 632.8 nm, beam diameter 1 mm, power 25.6 mW, and power meter Thorlabs PM100D. The position of the sample was such that the reflected light went at the minimum possible angle (that is, the power meter was located close to the radiation source, but did not block it). Then, the sample was folded 10 times around a standard metal rod with a diameter of 12 mm used to mount the optics. As a result of the folding, some cracks in polycarbonate itself were formed along the rod. The silver layer remains as is after the metasurface is rolled up. Then, the reflectivity was measured again. The metasurface after bending was scanned using AFM.

IV. RESULTS AND DISCUSSION

First, the flexible metasurfaces were characterized using ellipsometry. The results of ellipsometric measurements are shown in Fig. 8. The anomaly can be seen in the behavior of the polarization parameters Ψ and Δ. The discontinuity in the phase parameter $\Psi(\lambda)$ is observed in the spectral range from 540 to 780 nm. These wavelengths correspond to the green and near-infrared laser wavelengths used in Raman spectroscopy. The anomalous behavior is somewhat close to the first diffraction order that position is defined by the metasurface spacing and the incidence angle of light. The polarization anomaly in such a metasurface correlates with Wood's anomalies arising from the excitation of surface waves on the metasurface due to the diffraction of incident light by the periodic grating.

When studying flexible metasurfaces using the SNOM method, the topography was first obtained using the shear-force method [see Fig. 9(a)], after which the distribution of electromagnetic fields in this structure was studied [see

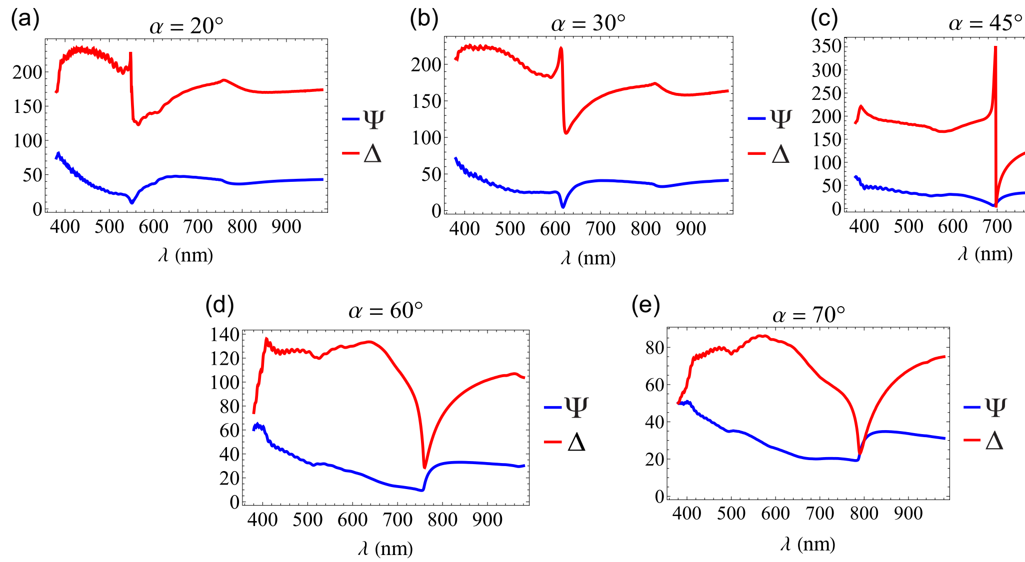

FIG. 8. Experimental ellipsometric parameters Ψ (blue lines) and Δ (red lines) for different angles of the incident light measured from the normal to the surface: (a) $\alpha = 20^\circ$, (b) $\alpha = 30^\circ$, (c) $\alpha = 45^\circ$, (d) $\alpha = 60^\circ$, and (e) $\alpha = 70^\circ$.

Fig. 9(b)]. To correlate the obtained data, red lines were drawn on the obtained images, which correspond to the direction of the grating period [see Figs. 9(a) and 9(b)]. In the obtained SNOM images, the minima of the electromagnetic field distribution pass along this line, which indicates that the field has a greater signal inside the

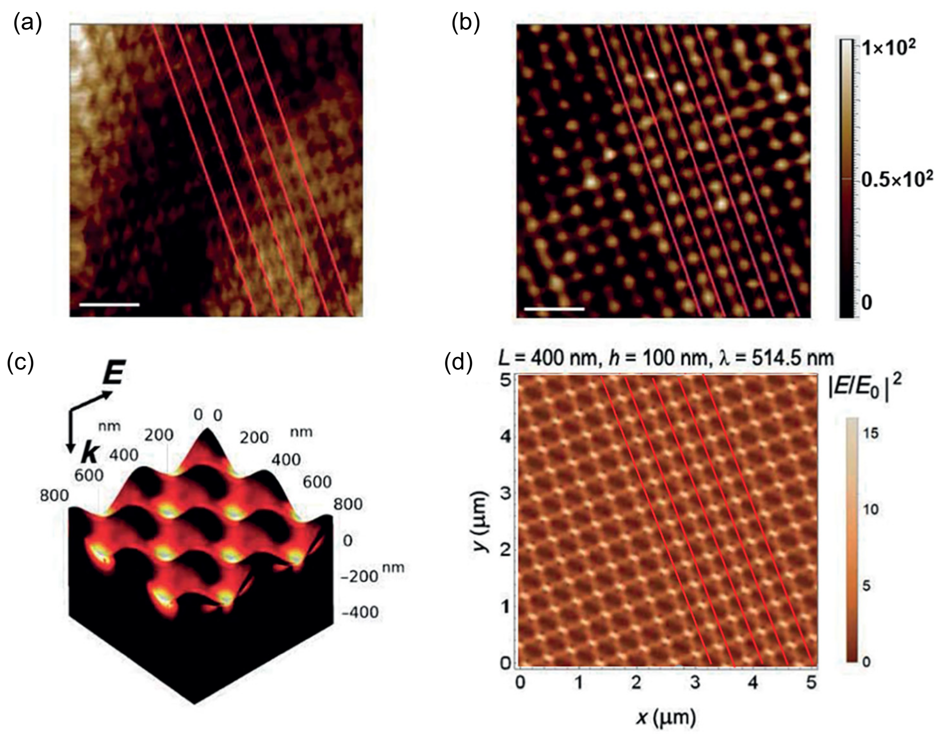

FIG. 9. (a) Topography AFM image of 5×5 μm^2 2D metasurface with silver thickness $d_{\max} = 65$ nm obtained by the shear-force method. (b) SNOM image of 5×5 μm^2 for the same section of the metasurface. Red lines along the lattice indicate the corresponding sections of the topography and SNOM images. The white horizontal scale bar is equal to 1 μm for (a),(b), the vertical scale in (b) is the relative value of the local electric field, and light dots correspond to maxima of the local electric field. (c),(d) COMSOL simulations of the distribution of the electric field intensity with $L = 400$ nm, $h = 100$ nm, $d_{\max} = 65$ nm, $d_{\max}/d_{\min} = 5$, and the light ($\lambda = 514.5$ nm) is incident normal to the metasurface for (c) eight elementary cells and (d) a zone of 5×5 μm^2.

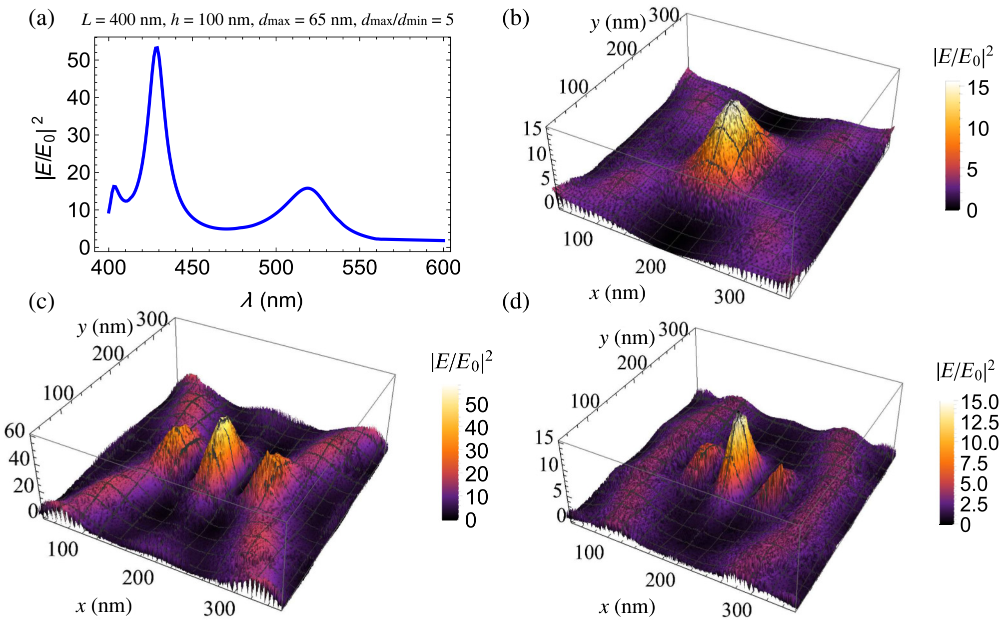

FIG. 10. (a) Computer simulation of electric field intensity in 2D metasurface (illumination under normal incidence); parameters are $L = 400$ nm, $h = 100$ nm, $d_{\max} = 65$ nm, and $d_{\max}/d_{\min} = 5$. Distributions of the electric field intensity corresponding to three resonances wavelengths: (b) $\lambda = 514.5$ nm, (c) $\lambda = 429$ nm, and (d) $\lambda = 403$ nm.

cells, and a minimum signal on the columns. 3D computer simulations were performed to investigate plasmon resonances in the double-periodic metal grating obtained by deposition of the thin silver film on the double-periodic dielectric substrate. We simulated the enhancement of the electric field in the modulated thin metal film with the same parameters of fabricated metasurface: period $L = 400$ nm, amplitude of the modulation $h = 100$ nm, silver thickness $d_{\max} = 65$ nm, and wavelength $\lambda = 514.5$ nm corresponding to the excitation wavelength used for SNOM pictures. Figure 9(c) shows the electric field distribution for eight simulated unit cells. Figure 9(d) shows the result of computer simulations of the distribution of the electric field intensity on a scale of 5×5 μm^2.

Figure 10 shows the electric field distribution for the first three resonances: dipolar resonance excited at a wavelength of 514.5 nm, and multipolar resonances excited at wavelengths of 429 and 403 nm. From Figs. 9(b) and 9(d), a good agreement was observed between the distribution of enhanced electric fields measured by SNOM and those obtained as a result of computer simulation. The results of SNOM experiments and computer modeling reliably state that enhanced local fields are focused precisely in the dents between the bumps forming the metasurface. In dents between the bumps, the metal film is continuously thin or can have a percolation structure in which plasmon resonances are excited near the percolation threshold. Moreover, electric field intensity is focused in a limited region, less than $\lambda/10$ in size, as depicted in Fig. 10. Thus, the presented metasurfaces can be considered as open resonators that excite short-wave plasmon modes. This circumstance is extremely important in SERS spectroscopy for the precise application of analyzed molecules to the localization region of enhanced plasmon fields. When studying metasurfaces for flexibility, the reflection coefficient before bending was 66% (16.9 mW out of 25.6 mW incident). Then, after bending, the reflectivity was measured again, which was 65% (16.7 mW out of 25.6 mW), indicating minor damage to the coating. The surface was examined using an optical microscope and AFM. AFM results showed that the polycarbonate itself was damaged, resulting in a 1.5-μm-deep crack, while the silver coating was not damaged (see Fig. 11). Preliminary results indicated that the metasurface bending resulted in a 1% change in reflectivity and did not result in a deterioration in the optical characteristics of the metasurface itself.

The developed flexible metasurfaces can be used where SERS analysis needs to be performed on uneven surfaces. Depending on the field of practical application, such double corrugated surfaces can be the surface of human or animal skin: for modern point-of-care real-time monitoring of various biomarkers such as glucose and glycated proteins in the blood, providing specific diagnosis of diabetes mellitus, renal failure, hypothyroidism [71–73]; cardiovascular markers for the diagnosis of acute myocardial infarction [74]; markers of neurodegenerative diseases such as Alzheimer's and Parkinson's [75,76]; tumor markers [77]; hormone estradiol E2 for the clinical diagnosis of precocious puberty [78]; and others. One of the main areas of practical use is highly sensitive rapid detection

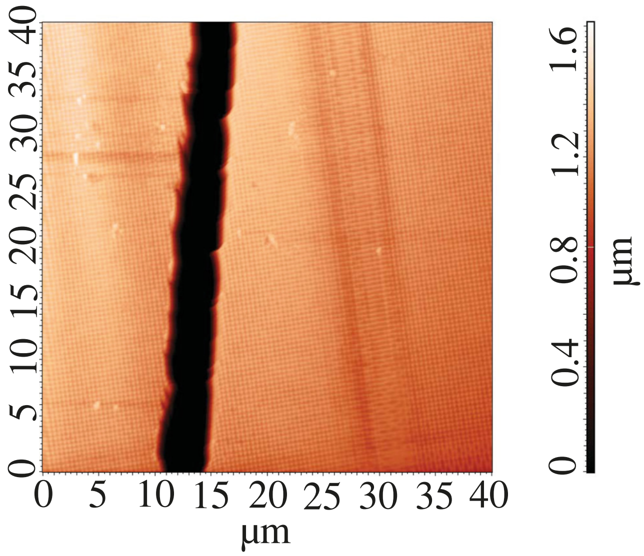

FIG. 11. AFM image of a crack after bending silver-coated metasurface 10 times.

of biopathogens, in particular monkey pox and SARS-CoV-2 coronavirus and its strains [79]. The morphology of the presented metasurfaces allows individual viruses with a size of 0.1 μm or more to be placed in cavities of comparable size, where enhanced fields are localized, thereby increasing the sensitivity of detection significantly. Such metasurfaces can be placed in liquids for environmental and food safety issues for real-time monitoring of pathogenic bacteria, pesticides, and toxic molecules. The problem of plastic waste released into the environment, such as soil and oceans, is particularly acute. Plastic residues can decompose into microplastic polymer particles with size less than 1 μm and nanoplastic particles of less than 100 nm. These particles can enter the body, including with food, and seriously affect health and quality of life. SERS metasurfaces can help detect small particles of microplastics and nanoplastics [80,81]. Another promising application is identification security marks. Flexible metasurfaces can be embedded in surfaces subject to bending for marking identity cards and documents, banknotes, strict reporting forms, and museum exhibits [82].

V. CONCLUSIONS

We have manufactured and investigated flexible metal-dielectric metasurfaces fabricated from modulated polycarbonate substrate coated by a thin silver film. Localization of optical excitation within subwavelength areas of the regular open-resonator metasurface has been observed by near-field scanning optical microscopy. The localized plasmons are seen as giant fluctuations of local electric fields spatially concentrated in hotspots. The local near-field spectra consisting of a regularly distributed strong resonance peaks have been detected. The form of the regularly distributed strong resonance peaks followed the topography of the metasurface. It has been shown that strong electromagnetic field concentrates in dents where the silver film has lowest thickness. Experimental results are in good agreement with results of the computer simulation of a double-periodic metal-dielectric metasurface and the predictions of the conformal map analytical theory. We believe that the presented metasurfaces can be stable and effective substrates for SERS and other optical spectroscopies.

ACKNOWLEDGMENT

This work was supported by the Russian Science Foundation under Grant No. 23-19-00788 [83].

[1] C.-C. Chang, W. J. Kort-Kamp, J. Nogan, T. S. Luk, A. K. Azad, A. J. Taylor, D. A. Dalvit, M. Sykora, and H.-T. Chen, High-temperature refractory metasurfaces for solar thermophotovoltaic energy harvesting, Nano Lett. **18**, 7665 (2018).

[2] L. Li, J. Wang, L. Kang, W. Liu, L. Yu, B. Zheng, M. L. Brongersma, D. H. Werner, S. Lan, Y. Shi *et al.*, Monolithic full-Stokes near-infrared polarimetry with chiral plasmonic metasurface integrated graphene–silicon photodetector, ACS Nano **14**, 16634 (2020).

[3] A. Pors, M. G. Nielsen, R. L. Eriksen, and S. I. Bozhevolnyi, Broadband focusing flat mirrors based on plasmonic gradient metasurfaces, Nano Lett. **13**, 829 (2013).

[4] J. Valentine, J. Li, T. Zentgraf, G. Bartal, and X. Zhang, An optical cloak made of dielectrics, Nat. Mater. **8**, 568 (2009).

[5] V. Fernández-Hurtado, F. J. García-Vidal, S. Fan, and J. C. Cuevas, Enhancing near-field radiative heat transfer with Si-based metasurfaces, Phys. Rev. Lett. **118**, 203901 (2017).

[6] A. Fedotova, M. Younesi, J. Sautter, A. Vaskin, F. J. Löchner, M. Steinert, R. Geiss, T. Pertsch, I. Staude, and F. Setzpfandt, Second-harmonic generation in resonant nonlinear metasurfaces based on lithium niobate, Nano Lett. **20**, 8608 (2020).

[7] A. S. Shorokhov, E. V. Melik-Gaykazyan, D. A. Smirnova, B. Hopkins, K. E. Chong, D.-Y. Choi, M. R. Shcherbakov, A. E. Miroshnichenko, D. N. Neshev, A. A. Fedyanin *et al.*, Multi-fold enhancement of third-harmonic generation in dielectric nanoparticles driven by magnetic fano resonances, Nano Lett. **16**, 4857 (2016).

[8] U. Aslam, S. Chavez, and S. Linic, Controlling energy flow in multimetallic nanostructures for plasmonic catalysis, Nat. Nanotechnol. **12**, 1000 (2017).

[9] J. Qin, S. Jiang, Z. Wang, X. Cheng, B. Li, Y. Shi, D. P. Tsai, A. Q. Liu, W. Huang, and W. Zhu, Metasurface micro/nano-optical sensors: Principles and applications, ACS Nano **16**, 11598 (2022).

[10] M. Song, L. Feng, P. Huo, M. Liu, C. Huang, F. Yan, Y.-Q. Lu, and T. Xu, Versatile full-color nanopainting enabled by a pixelated plasmonic metasurface, Nat. Nanotechnol. **18**, 71 (2023).

[11] S. N. Chowdhury, J. Simon, M. P. Nowak, K. Pagadala, P. Nyga, C. Fruhling, E. G. Bravo, S. Mackowski, V. M.

Shalaev, A. V. Kildishev, and A. Boltasseva, Wide-range angle-sensitive plasmonic color printing on lossy-resonator substrates, Adv. Opt. Mater. **12**, 2301678 (2023).

[12] A. A. Lisyansky, E. S. Andrianov, A. P. Vinogradov, and V. Y. Shishkov, in *Quantum Optics of Light Scattering* (Springer International Publishing, Cham, 2024), p. 217.

[13] S. Lee, H. Dang, J.-I. Moon, K. Kim, Y. Joung, S. Park, Q. Yu, J. Chen, M. Lu, L. Chen, S.-W. Joo, and J. Choo, SERS-based microdevices for use as in vitro diagnostic biosensors, Chem. Soc. Rev. **53**, 5394 (2024).

[14] K. Ou, H. Wan, G. Wang, J. Zhu, S. Dong, T. He, H. Yang, Z. Wei, Z. Wang, and X. Cheng, Advances in meta-optics and metasurfaces: Fundamentals and applications, Nanomaterials **13**, 1235 (2023).

[15] G. Barbillon, Latest advances in metasurfaces for SERS and SEIRA sensors as well as photocatalysis, Int. J. Mol. Sci. **23**, 10592 (2022).

[16] V. V. Klimov, Optical nanoresonators, Phys.-Usp. **66**, 263 (2023).

[17] J. Henzie, J. Lee, M. H. Lee, W. Hasan, and T. W. Odom, Nanofabrication of plasmonic structures, Annu. Rev. Phys. Chem. **60**, 147 (2009).

[18] Q. Yu, P. Guan, D. Qin, G. Golden, and P. M. Wallace, Inverted size-dependence of surface-enhanced Raman scattering on gold nanohole and nanodisk arrays, Nano Lett. **8**, 1923 (2008).

[19] A.-C. Faure, G. Barbillon, M. Ou, G. Ledoux, O. Tillement, S. Roux, D. Fabregue, A. Descamps, J.-L. Bijeon, C. A. Marquette, C. Billotey, C. Jamois, T. Benyatou, and P. Perriat, Core/shell nanoparticles for multiple biological detection with enhanced sensitivity and kinetics, Nanotechnology **19**, 485103 (2008).

[20] P. Zhang, S. Yang, L. Wang, J. Zhao, Z. Zhu, B. Liu, J. Zhong, and X. Sun, Large-scale uniform Au nanodisk arrays fabricated via X-ray interference lithography for reproducible and sensitive SERS substrate, Nanotechnology **25**, 245301 (2014).

[21] T. Gong, Y. Luo, C. Zhao, W. Yue, J. Zhang, Y. Zhu, M. Pu, Z. Zuojun, C. Wang, and X. Luo, Highly reproducible and stable surface-enhanced Raman scattering substrates of graphene-Ag nanohole arrays fabricated by sub-diffraction plasmonic lithography, OSA Contin. **2**, 582 (2019).

[22] G. Barbillon, J.-L. Bijeon, G. Lérondel, J. Plain, and P. Royer, Detection of chemical molecules with integrated plasmonic glass nanotips, Surf. Sci. **602**, L119 (2008).

[23] A. Dhawan, A. Duval, M. Nakkach, G. Barbillon, J. Moreau, M. Canva, and T. Vo-Dinh, Deep UV nano-microstructuring of substrates for surface plasmon resonance imaging, Nanotechnology **22**, 165301 (2011).

[24] T. Ding, D. O. Sigle, L. O. Herrmann, D. Wolverson, and J. J. Baumberg, Nanoimprint lithography of al nanovoids for deep-UV SERS, ACS Appl. Mater. Interfaces **6**, 17358 (2014).

[25] J.-F. Masson, K. F. Gibson, and A. Provencher-Girard, Surface-enhanced Raman spectroscopy amplification with film over etched nanospheres, J. Phys. Chem. C **114**, 22406 (2010).

[26] A. K. Sarychev, A. Ivanov, A. N. Lagarkov, I. Ryzhikov, K. Afanasev, I. Bykov, G. Barbillon, N. Bakholdin, M. Mikhailov, A. Smyk *et al.*, Plasmon localization and giant fields in an open-resonator metasurface for surface-enhanced-Raman-scattering sensors, Phys. Rev. Appl. **17**, 044029 (2022).

[27] M. Kraft, Y. Luo, S. A. Maier, and J. B. Pendry, Designing plasmonic gratings with transformation optics, Phys. Rev. X **5**, 1 (2015).

[28] A. Ivanov, A. K. Sarychev, I. V. Bykov, I. Boginskaya, A. Lagarkov, I. Ryzhikov, N. Nechaeva, and I. Kurochkin, Silicon-silver metasurface based on regular bars as an effective SERS substrate, J. Phys.: Conf. Ser. **1461**, 012057 (2020).

[29] S. K. Verma and S. K. Srivastava, Experimental demonstration of a Fano resonant hybrid plasmonic metasurface absorber for the O and E bands of the optical communication window, JOSA B **41**, 356 (2024).

[30] D. Chowdhury, M. C. Giordano, G. Manzato, R. Chittofrati, C. Mennucci, and F. Buatier de Mongeot, Large-area microfluidic sensors based on flat-optics Au nanostripe metasurfaces, J. Phys. Chem. C **124**, 17183 (2020).

[31] C. Xiao, Z. Chen, M. Qin, D. Zhang, and L. Fan, Composite sinusoidal nanograting with long-range SERS effect for label-free TNT detection, Photonic Sens. **8**, 278 (2018).

[32] X. Luo and T. Ishihara, Surface plasmon resonant interference nanolithography technique, Appl. Phys. Lett. **84**, 4780 (2004).

[33] X. Chen, F. Yang, C. Zhang, J. Zhou, and L. J. Guo, Large-area high aspect ratio plasmonic interference lithography utilizing a single high-k mode, ACS Nano **10**, 4039 (2016).

[34] K. Dixon, X. Zhu, L. Chen, A. Montazeri, N. Matsuura, N. P. Kherani, and H.-Y. N. Holman, Dispersion-engineered deep sub-wavelength plasmonic metasurfaces for broadband Seira applications, Adv. Opt. Mater. **12**, 2300979 (2024).

[35] A. C. Tasolamprou, E. Skoulas, G. Perrakis, M. Vlahou, Z. Viskadourakis, E. N. Economou, M. Kafesaki, G. Kenanakis, and E. Stratakis, Highly ordered laser imprinted plasmonic metasurfaces for polarization sensitive perfect absorption, Sci. Rep. **12**, 19769 (2022).

[36] F. Saeed, T. Iqbal, N. Al-Zaqri, I. Warad, and M. S. Sultan, Modelling and optimization of 1D sinusoidal plasmonic grating application in solar cell, Plasmonics **18**, 1117 (2023).

[37] A. Cordaro, H. Kwon, D. Sounas, A. F. Koenderink, A. Alù, and A. Polman, High-index dielectric metasurfaces performing mathematical operations, Nano Lett. **19**, 8418 (2019).

[38] S. Choi, J. Zuo, N. Das, Y. Yao, and C. Wang, Scalable nanoimprint manufacturing of functional multilayer metasurface devices, Adv. Funct. Mater. **34**, 2404852 (2024).

[39] A. K. Sarychev, A. N. Lagarkov, A. V. Ivanov, A. V. Boginskaya, I. V. Bykov, I. A. Ryzhikov, M. V. Sedova, A. V. Vaskin, I. N. Kurochkin, I. A. Rodionov, and D. V. Negrov, in *Proc. of SPIE, Plasmonics: Design, Materials, Fabrication, Characterization, and Applications XV* (SPIE, San Diego, US, 2017), Vol. 10346, p. 103460C.

[40] A. K. Sarychev, A. N. Lagarkov, A. V. Ivanov, K. N. Afanasyev, I. V. Bykov, A. N. Lagarkov, A. M. Merzlikin, V. V. Mikheev, D. V. Negrov, I. A. Ryzhikov, and M. V. Sedova, Enhancement of local electromagnetic fields by periodic optical resonators, Quantum Electron. **48**, 1147 (2018).

[41] S. I. Azzam, V. M. Shalaev, A. Boltasseva, and A. V. Kildishev, Formation of bound states in the continuum in hybrid plasmonic-photonic systems, Phys. Rev. Lett., **121**, 253901 (2018).

[42] A. N. Lagarkov, I. Boginskaya, I. Bykov, I. Budashov, A. Ivanov, I. Kurochkin, I. Ryzhikov, I. Rodionov, M. Sedova, A. Zverev, and A. K. Sarychev, Light localization and SERS in tip-shaped silicon metasurface, Opt. Express **25**, 17021 (2017).

[43] Y. Chen, H. Yin, D. Sikdar, L. Yan, Z. Zhou, J. Sun, and C. Wang, Gold nanopolyhedron-based superlattice sheets as flexible surface-enhanced Raman scattering sensors for detection of 4-aminothiophenol, ACS Appl. Nano Mater. **4**, 12498 (2021).

[44] G. Palermo, M. Rippa, Y. Conti, A. Vestri, R. Castagna, G. Fusco, E. Suffredini, J. Zhou, J. Zyss, A. De Luca, and L. Petti, Plasmonic metasurfaces based on pyramidal nanoholes for high-efficiency SERS biosensing, ACS Appl. Mater. Interfaces **13**, 43715 (2021).

[45] M. Rippa, D. Sagnelli, A. Vestri, V. Marchesano, B. Munari, D. Carnicelli, E. Varrone, M. Brigotti, R. Tozzoli, M. Montalbano, S. Morabito, J. Zhou, J. Zyss, and L. Petti, Plasmonic metasurfaces for specific SERS detection of Shiga toxins, ACS Appl. Mater. Interfaces **14**, 4969 (2022).

[46] V. Caligiuri, G. Tedeschi, M. Palei, M. Miscuglio, B. Martin-Garcia, S. Guzman-Puyol, M. K. Hedayati, A. Kristensen, A. Athanassiou, R. Cingolani, V. J. Sorger, M. Salerno, F. Bonaccorso, R. Krahne, and J. A. Heredia-Guerrero, Biodegradable and insoluble cellulose photonic crystals and metasurfaces, ACS Nano **14**, 9502 (2020).

[47] U. R. Gabinet and C. O. Osuji, Plasmonic sensing from vertical Au-coated ZnO nanorod arrays templated by block copolymers, ACS Appl. Nano Mater. **4**, 8556 (2021).

[48] K. Yang, J. Wang, X. Yao, D. Lyu, J. Zhu, Z. Yang, B. Liu, and B. Ren, Large-area plasmonic metamaterial with thickness-dependent absorption, Adv. Opt. Mater. **9**, 2001375 (2021).

[49] Y. Zhao, A. Hubarevich, M. Iarossi, T. Borzda, F. Tantussi, J.-A. Huang, and F. De Angelis, Hyperbolic nanoparticles on substrate with separate optical scattering and absorption resonances: A dual function platform for SERS and thermoplasmonics, Adv. Opt. Mater. **9**, 2100888 (2021).

[50] Y. Ma, D. Sikdar, A. Fedosyuk, L. Velleman, D. J. Klemme, S.-H. Oh, A. R. J. Kucernak, A. A. Kornyshev, and J. B. Edel, Electrotunable nanoplasmonics for amplified surface enhanced Raman spectroscopy, ACS Nano **14**, 328 (2020).

[51] N. P. Kovalets, E. P. Kozhina, I. V. Razumovskaya, S. A. Bedin, A. A. Piryazev, Y. V. Grigoriev, and A. V. Naumov, Toward single-molecule surface-enhanced Raman scattering with novel type of metasurfaces synthesized by crack-stretching of metallized track-etched membranes, J. Chem. Phys. **156**, 034902 (2022).

[52] T. V. Nguyen, L. T. Pham, B. X. Khuyen, D. C. Duong, L. H. T. Nghiem, N. T. Nguyen, D. Vu, D. Q. Hoa, V. D. Lam, and H. M. Nguyen, Effects of metallic underlayer on SERS performance of a metal film over nanosphere metasurface, J. Phys. D: Appl. Phys. **55**, 025101 (2022).

[53] P. Mao, C. Liu, Q. Chen, M. Han, S. A. Maier, and S. Zhang, Broadband SERS detection with disordered plasmonic hybrid aggregates, Nanoscale **12**, 93 (2020).

[54] Y. Wang, C. Zhao, J. Wang, X. Luo, L. Xie, S. Zhan, J. Kim, X. Wang, X. Liu, and Y. Ying, Wearable plasmonic-metasurface sensor for noninvasive and universal molecular fingerprint detection on biointerfaces, Sci. Adv. **7**, eabe4553 (2021).

[55] S. Luo, A. Mancini, R. Berté, B. H. Hoff, S. A. Maier, and J. C. de Mello, Massively parallel arrays of size-controlled metallic nanogaps with gap-widths down to the sub-3-nm level, Adv. Mater. **33**, 2100491 (2021).

[56] S. J. Bauman, A. A. Darweesh, M. Furr, M. Magee, C. Argyropoulos, and J. B. Herzog, Tunable SERS enhancement via sub-nanometer gap metasurfaces, ACS Appl. Mater. Interfaces **14**, 15541 (2022).

[57] W. Zhang, B. Ai, P. Gu, Y. Guan, Z. Wang, Z. Xiao, and G. Zhang, Plasmonic chiral metamaterials with sub-10 nm nanogaps, ACS Nano **15**, 17657 (2021).

[58] V. Thareja, M. Esfandyarpour, P. G. Kik, and M. L. Brongersma, Anisotropic metasurfaces as tunable SERS substrates for 2D materials, ACS Photonics **6**, 1996 (2019).

[59] T. Jiang, P. Goel, H. Zhao, R. Ma, L. Zhu, X. Liu, and L. Tang, Metasurfaces: Internal structure tailoring in 3D nanoplasmonic metasurface for surface-enhanced Raman spectroscopy, Part. Part. Syst. Charact. **37**, 1900345 (2020).

[60] D. Paria, K. S. Kwok, P. Raj, P. Zheng, D. H. Gracias, and I. Barman, Label-free spectroscopic SARS-CoV-2 detection on versatile nanoimprinted substrates, Nano Lett. **22**, 3620 (2022).

[61] K. Wang, D.-W. Sun, H. Pu, Q. Wei, and L. Huang, Stable, flexible, and high-performance SERS chip enabled by a ternary film-packaged plasmonic nanoparticle array, ACS Appl. Mater. Interfaces **11**, 29177 (2019).

[62] V. Narasimhan, R. H. Siddique, H. Park, and H. Choo, Bioinspired disordered flexible metasurfaces for human tear analysis using broadband surface-enhanced Raman scattering, ACS Omega **5**, 12915 (2020).

[63] M. S. S. Bharati and V. R. Soma, Flexible SERS substrates for hazardous materials detection: Recent advances, Opto-Electron. Adv. **4**, 210048 (2021).

[64] H. Cui, S. Li, S. Deng, H. Chen, and C. Wang, Flexible, transparent, and free-standing silicon nanowire SERS platform for in situ food inspection, ACS Sens. **2**, 386 (2017).

[65] K. Xu, R. Zhou, K. Takei, and M. Hong, Toward flexible surface-enhanced Raman scattering (SERS) sensors for point-of-care diagnostics, Adv. Sci. **6**, 1900925 (2019).

[66] P. A. Huidobro, Y. H. Chang, M. Kraft, and J. B. Pendry, Hidden symmetries in plasmonic gratings, Phys. Rev. B **95**, 1 (2017).

[67] J. B. Pendry, P. A. Huidobro, Y. Luo, and E. Galiffi, Compacted dimensions and singular plasmonic surfaces, Science **358**, 915 (2017).

[68] J. B. Pendry, P. A. Huidobro, and K. Ding, Computing one dimensional metasurfaces, Phys. Rev. B **99**, 085408 (2019).

[69] P. B. Johnson and R. W. Christy, Optical constants of the noble metals, Phys. Rev. B **6**, 4370 (1972).

[70] G. Barbillon, A. Ivanov, and A. K. Sarychev, Hybrid Au/Si disk-shaped nanoresonators on gold film for amplified SERS chemical sensing, Nanomaterials **9**, 1588 (2019).

[71] X. Sun, Glucose detection through surface-enhanced Raman spectroscopy: A review, Anal. Chim. Acta **1206**, 339226 (2022).

[72] N. C. Dingari, G. L. Horowitz, J. W. Kang, R. R. Dasari, and I. Barman, Raman spectroscopy provides a powerful diagnostic tool for accurate determination of albumin glycation, PLoS One **7**, e32406 (2012).

[73] J. Lin, J. Lin, Z. Huang, P. Lu, J. Wang, X. Wang, and R. Chen, Raman spectroscopy of human hemoglobin for diabetes detection, J. Innov. Opt. Health Sci. **7**, 1350051 (2014).

[74] M. Naz, H. Shafique, M. I. Majeed, H. Nawaz, N. Rashid, A. Alshammari, N. A. Albekairi, A. Amber, M. Zohaib, U. Shahid, F. Zafar, M. Ali, and H. Shahid, Surface-enhanced Raman spectroscopy (SERS) for the diagnosis of acute myocardial infarction (AMI) using blood serum samples, RSC Adv. **14**, 29151 (2024).

[75] M. Kim, S. Huh, H. J Park, S. H Cho, M. Y Lee, S. Jo, and Y. S Jung, Surface-functionalized SERS platform for deep learning-assisted diagnosis of Alzheimer's disease, Biosens. Bioelectron. **251**, 116128 (2024).

[76] S. Ge, G. Chen, J. Deng, Y. Gu, Y. Mao, X. Zhou, and G. Li, Multiplex signal amplification strategy-based early-stage diagnosis of Parkinson's disease on a SERS-enabled LoC system, Anal. Chim. Acta **1247**, 340890 (2023).

[77] J. Kneipp, Interrogating cells, tissues, and live animals with new generations of surface-enhanced Raman scattering probes and labels, ACS Nano **11**, 1136 (2017).

[78] R. Wang, H. Chon, S. Lee, Z. Cheng, S. H. Hong, Y. H. Yoon, and J. Choo, Highly sensitive detection of hormone estradiol E2 using surface-enhanced Raman scattering based immunoassays for the clinical diagnosis of precocious puberty, ACS Appl. Mater. Interfaces **8**, 10665 (2016).

[79] A. K. Sarychev, A. Sukhanova, A. V. Ivanov, I. V. Bykov, N. V. Bakholdin, D. V. Vasin, V. A. Gushchin, A. P. Tkachuk, G. Nifontova, P. S. Samokhvalov, A. Karaulov, and I. Nabiev, Label-free detection of the receptor-binding domain of the SARS-CoV-2 spike glycoprotein at physiologically relevant concentrations using surface-enhanced Raman spectroscopy, Biosensors **12**, 300 (2022).

[80] L. Mikac, I. Rigó, L. Himics, A. Tolić, M. Ivanda, and M. Veres, Surface-enhanced Raman spectroscopy for the detection of microplastics, Appl. Surf. Sci. **608**, 155239 (2023).

[81] T. Dey, Microplastic pollutant detection by surface enhanced Raman spectroscopy (SERS): A mini-review, Nanotechnol. Environ. Eng. **8**, 41 (2023).

[82] A. P. Gubarev, A. N. Shalygin, A. K. Sarychev, A. V. Ivanov, I. V. Bykov, A. S. Kuznetsov, S. B. Odinokov, and A. F. Smyk, Using molecular marking in security holograms, J. Opt. Technol. **89**, 155 (2022).

[83] https://rscf.ru/project/23-19-00788/